

See discussions, stats, and author profiles for this publication at: <https://www.researchgate.net/publication/264636619>

Single-Sheeted Double Many-Body Expansion Potential Energy Surface for Ground-State ClO₂

ARTICLE *in* THE JOURNAL OF PHYSICAL CHEMISTRY A · JUNE 2014

Impact Factor: 2.69 · DOI: 10.1021/jp503744x · Source: PubMed

CITATION

1

READS

56

4 AUTHORS, INCLUDING:



[Antonio J. C. Varandas](#)

University of Coimbra

382 PUBLICATIONS 6,742 CITATIONS

SEE PROFILE

Single-Sheeted Double Many-Body Expansion Potential Energy Surface for Ground-State ClO₂

O. B. M. Teixeira,[†] V. C. Mota,[‡] J. M. Garcia de la Vega,[†] and A. J. C. Varandas^{*,§,‡}

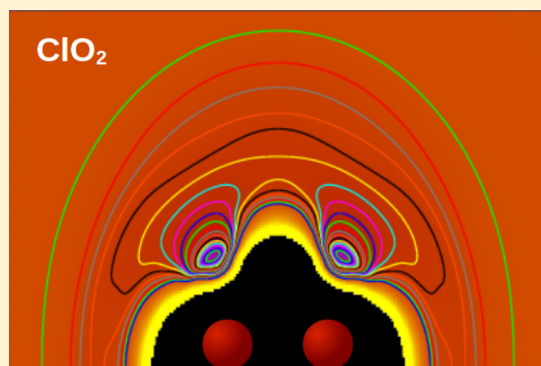
[†]Departamento de Química Física Aplicada, Universidad Autónoma de Madrid, 28049 Madrid, Spain

[‡]Departamento de Física, Universidade Federal do Espírito Santo, 29075-910 Vitória, Brazil

[§]Centro de Química, and Departamento de Química, Universidade de Coimbra, 3004-535 Coimbra, Portugal

Supporting Information

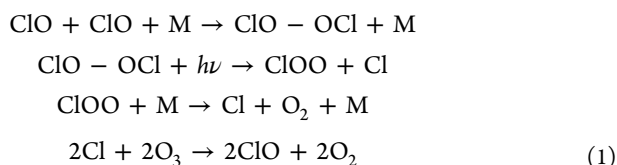
ABSTRACT: A global single-sheeted double many-body expansion potential energy surface is reported for the ground electronic state of ClO₂. The potential energy surface is obtained by fitting 3200 energy points that map all atom–diatom dissociation channels as well as all relevant stationary points, including the well-known OCIO and CIOO structures. The ab initio calculations are obtained at the multireference configuration interaction level of theory, employing the cc-pVXZ (*X* = *D*, *T*) Dunning basis sets, and then extrapolated to the complete basis set limit with the generalized uniform singlet- and triplet-pair protocol. The topographical features of the novel global potential energy surface are examined in detail.



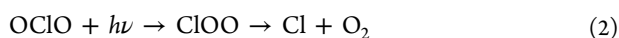
1. INTRODUCTION

In the last decades, the chemistry of chlorine and other halogen species has become of central relevance because of its importance in atmospheric chemistry.^{1,2} The ozone depletion observed in the stratospheric polar vortex above Antarctica has been found to be primarily caused by catalytic ozone-destroying reaction cycles involving reactive halogen-free radicals.³ Therefore, the suggestion that antropogenic sources of chlorine were responsible for the transport and subsequent production of atomic chlorine in the stratosphere provided the impetus for studies designed to understand the halogen-based chemistry that results in ozone loss.⁴

In the stratosphere each chlorine atom can remove as many as 10⁶ ozone molecules before disappearance,⁵ and the chemical reactions responsible for this process would involve among other species the chlorine dioxides isomers, CIOO, and symmetric OCIO. In fact, in the polar stratosphere, ozone is taught to be depleted by the catalytic cycle^{6–8} involving the CIOO species



which has as a net effect $2\text{O}_3 \rightarrow 3\text{O}_2$. Cl atoms, which deplete ozone via reaction $\text{Cl} + \text{O}_3 \rightarrow \text{ClO} + \text{O}_2$, may also be produced through the reaction^{9,10}



in which OCIO undergoes photoisomerization into CIOO. Note that OCIO preferentially photodissociates into OCl + O, therefore forming cyclic processes with null net effect on the ozone depletion since the oxygen atoms upon reaction with O₂ molecules yields O₃. However, it is now accepted that the Cl atoms produced by the process in eq 2 may be relevant for ozone depletion, even if not produced in relatively large proportions.

The importance of the CIOO and OCIO species in the ozone depletion has been established only after a significant amount of theoretical and experimental work. As an attempt to theoretically elucidate the photodynamics of OCIO in face of the large amount of spectroscopic results available,^{11–16} Peterson and Werner^{17,18} have devised an extensive ab initio multiconfigurational study of the ClO₂ molecule. Combining the internally contracted version of the multireference configuration interaction (MRCI) method^{19,20} using orbitals optimized at the complete active space self-consistent field (CASSCF) level of theory^{21,22} with the correlation consistent polarized valence quadruple- ζ (cc-pVXZ, with *X* = *Q*) basis set of Dunning,^{23,24} local potential energy surfaces (PESs) for the ²A₁, ²A₂, and ²B₂ (C_{2v}) and ¹2A', ²2A', and ¹2A'' (C_s) electronic states have been constructed.^{17,18} Electric dipole moments have also been obtained, with good agreement with previous experimental work²⁵ being reported.¹⁷ The channels leading into the dissociation OCIO → OCl + O have been

Received: April 16, 2014

Revised: June 10, 2014



characterized,¹⁷ and the OCIO + $h\nu$ → CIOO process studied in detail.¹⁸ Regarding the Cl + O₂ production in eq 2, good agreement with the photofragment translational energy spectroscopy results of Davis and Lee²⁶ has been reported, therefore revealing that the OCIO + $h\nu$ → CIOO photoisomerization may be well-described by multiconfigurational methods. Subsequent experimental measurements employing femtosecond spectroscopy²⁷ also appear to corroborate their results.^{17,18} More recently, Meng and Huang²⁸ revisited the photochemistry of OCIO. Using multiconfigurational second-order perturbation theory (CASPT2)²⁹ jointly with an atomic natural orbital (ANO-L)^{30–33} basis set, they have proposed predissociation mechanisms different than those first proposed by Peterson and Werner^{17,18} to be involved both in the OCIO → OCl + O dissociation and OCIO → CIOO photoisomerization. Other studies have been dedicated to investigate aspects other than the photochemistry of OCIO. Employing similar ab initio methodologies as used in previous work,¹⁷ Peterson and Werner³⁴ constructed local PESs for the first seven electronic states of OCIO⁺ and for the ground X¹A₁ electronic state of OCIO⁺ to investigate spectroscopic properties of such species. In turn, Peterson³⁵ constructed local PESs for the X²B₁ and ²A₂ electronic states of OCIO and reported agreement with experimental results for spectroscopic constants and vibrational states up to 5 cm^{−1}. Grant et al.³⁶ have included the OCIO and CIOO species in a detailed ab initio investigation of the thermodynamic properties of halogen oxides based on coupled cluster theory and the correlated consistent basis sets of Dunning, obtaining accurate results for properties such as total atomization energies, geometries, frequencies, heats of formation, and bond dissociation energies. Additionally, Wei et al.³⁷ have reported an extensive ab initio study of the spectroscopic properties of several excited states of the OCIO radical as well as of its anion and cation, employing CASPT2/CASSCF methods with a large atomic natural orbital (ANO-L) basis set. They have given equilibrium structures, ionization potentials, detachment energies, and absorption spectra of up to 10, 13, and 9 electronic states of OCIO, OCIO⁺, and OCIO[−], respectively. Higher valence and Rydberg excited states of OCIO have also been studied by Grein.³⁸ The MRCI level of theory jointly with the valence triple- ζ plus double polarization (TZVPP) basis set³⁹ have been employed, and good agreement with experimental results has been reported for the calculated energies and oscillator strengths.

Regarding the CIOO species, theoretical attention has been paid to the characterization of the CIOO electronic ground state properties via single reference methods,^{36,40,41} density functional theory (DFT),^{42–45} and multireference studies.^{17,46–49} Among the single reference studies, we highlight the extensive calculations on XO₂, XOOX, XO_{*m*}, and HXO_{*n*} for X = F and Cl molecules by Karton et al.⁴¹ aiming at obtaining benchmark results for the thermochemistry properties of halogen oxides. Employing the so-called W4 computational thermochemistry protocol,^{50–53} equilibrium structures, total atomization energies, and more importantly, nondynamical correlation (NDC) diagnostics are investigated in detail, showing the importance of properly accounting for NDC in both the CIOO and OCIO species. Similar conclusions have been obtained by Suma et al. when studying^{47,48} both the CIOO spectroscopy⁴⁷ and CIOO formation from Cl plus O₂.⁴⁸ In the computational part of their work, they have employed the MRCI/CASSCF level of theory with three distinct active spaces in the CASSCF wave function and the Davidson

correction (MRCI + Q/CASSCF) jointly with aug-cc-pVXZ (X = D, T, Q and 5) basis sets, followed by extrapolation to the complete basis set (CBS) limit to determine both the Cl–O₂ bond dissociation energy and structural parameters. They reported a very strong dependence on the size of both the basis set and the active space when describing the weak Cl–O bond well depth with respect to the Cl + O₂ channel. Although for active spaces larger than used in previous work¹⁷ their calculated value⁴⁸ of $D_0 = 4.65$ kcal mol^{−1} gets closer to their own experimental value⁴⁸ of $D_0 = 4.69$ kcal mol^{−1}, an even larger active space would be needed to match the experiment since spin–orbit coupling (neglected in all their calculations^{47,48}) would raise the difference relative to the experimental well depth by ≈ 1.0 kcal mol^{−1}.

Regarding the reaction dynamics of the bimolecular processes occurring in the CIO₂ PES, Zhu and Lin⁴⁵ used DFT method to map the CIO₂ configuration space and subsequently obtain rate constants using transition state theory (TST). They have employed the PW91PW91/6-311 + G(3 df) functional⁴⁵ to investigate the isomerization and decomposition of the CIOO and OCIO radicals, and the GM2 method⁵⁴ for predicting bond-dissociation energies and harmonic vibrational frequencies, reporting quite satisfactory with experimental results.^{55,56}

Given the relevance of both OCIO and CIOO species for the chemistry of halogen atoms in the atmosphere and the central role that multiconfigurational methods would play in any related study, in this work we report the first realistic global PES for the ground electronic state of CIO₂ based on the double many-body expansion^{57–60} (DMBE) method (for recent progress on the methodology, see elsewhere⁶¹). The analytic CIO₂ DMBE PES has been calibrated from approximately 3200 ab initio points that were calculated at the MRCI/cc-pVXZ (with X = D,T) level of theory. The PES so obtained shows the correct long-range behavior at all dissociation channels and provides a realistic representation of the surface features at all interatomic separations (e.g., van der Waals wells at intermediate atom–diatom separations). The paper is organized as follows: Computational Details describes the ab initio calculations carried out in the present work, and DMBE Potential Energy Surface for CIO₂ deals with the analytical representation of the PES. The main topographical features of the DMBE PES are discussed in Main Features of the Potential Energy Surface. Some concluding remarks are gathered in section 5.

2. COMPUTATIONAL DETAILS

The calculations have been performed using the internally contracted version of the MRCI¹⁹ method with the Davidson correction (MRCI + Q) using a CASSCF wave function²¹ as reference and two basis sets, namely^{23,24} cc-pVDZ and cc-pVTZ or simply VDZ and VTZ. Some MRCI + Q calculations have also been performed with the VQZ basis, as described later. The active space is formed from the 12 molecular orbitals obtained from the 2s and 2p atomic orbitals of oxygen and the 3s and 3p atomic orbitals of chlorine, correlating a total of 19 active electrons. All calculations have been performed with the Molpro package⁶² for ab initio electronic structure calculations. Approximately 3200 grid points have been computed to map the PES over the region defined by $1.8 \leq R_1/a_0 \leq 8.0$, $0.5 \leq r_1/a_0 \leq 10.0$, and $0.0 \leq \gamma_1/\text{deg} \leq 90$, for Cl–O₂ interactions, and by $1.8 \leq R_2/a_0 \leq 8.0$, $0.5 \leq r_2/a_0 \leq 10.0$, and $0.0 \leq \gamma_2/\text{deg} \leq 180$, for O–ClO interactions; r , R , and γ are the corresponding

atom–diatom Jacobi coordinates defined in Figure 1. The ab initio data used to construct the O₂ diatomic potential consists

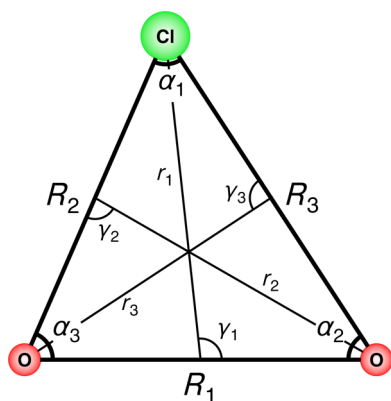


Figure 1. Coordinates used in the present work.

of Cl – O₂ calculations with the r_1 and γ_1 coordinates fixed at $10.0a_0$ and 90 deg, respectively, while the R_1 coordinate varies within the range $1.8 \leq R_1/a_0 \leq 8.0$. Similarly, to obtain the ClO ab initio data we have kept the r_2 and γ_2 coordinates fixed at $10.0a_0$ and 90 deg, respectively, in O–ClO calculations while varying the R_2 distance within the range $1.8 \leq R_2/a_0 \leq 8.0$. As noted above, a profile of similar calculations has also been carried out for test purposes at the MRCI + Q/VQZ level of theory. It involves a total of 30 geometries with a fixed ClO bond distance of $R_2 = 3.0a_0$, and a fixed Jacobi angle of $\gamma_2 = 135$ deg, with the atom–diatom varying between $2.20a_0$ and $9.45a_0$ at intervals of $0.25a_0$. Aiming at an extrapolation of the calculated raw ab initio energies to the CBS limit, the following test calculations have been performed. First, the MRCI/VXZ ($X = D$ and T) raw correlation energies were extrapolated along the above profile for the $(m + 1)$ -th basis set (i.e., VQZ) using the correlation scaling (CS) procedure suggested by Varandas and Piecuch.^{63,64} In its simplest formulation, the scaled correlation is obtained as⁶³

$$E_{m+1}(\mathbf{R}) = E_{m+1}^{\text{ref}}(\mathbf{R}) + \chi_{m+1,m}(\mathbf{R})\Delta E_m(\mathbf{R}) \quad (3)$$

where $E_{m+1}^{\text{ref}}(\mathbf{R})$ is the CASSCF energy of the reference wave function with the $(m + 1)$ th basis set,

$$\Delta E_m(\mathbf{R}) = E_m(\mathbf{R}) - E_m^{\text{ref}}(\mathbf{R}) \quad (4)$$

\mathbf{R} the τ -dimensional vector of the nuclear space coordinates defining the PES, and

$$\chi_{m+1,m}(\mathbf{R}) = 1 + \frac{S(\mathbf{R})_{m,m-1} - 1}{S(\mathbf{R}_e)_{m,m-1} - 1} [S(\mathbf{R}_e)_{m+1,m} - 1] \quad (5)$$

with $S(\mathbf{R})_{m,m-1} = \Delta E_m(\mathbf{R})/\Delta E_{m-1}(\mathbf{R})$. The reference geometry \mathbf{R}_e can be either the equilibrium geometry or any other point on the PES. Thus, the MRCI PES $E_{m+1}(\mathbf{R})$ is extrapolated from the PESs $E_m(\mathbf{R})$ and $E_{m-1}(\mathbf{R})$, the reference energies $E_{m+1}^{\text{ref}}(\mathbf{R})$, $E_m^{\text{ref}}(\mathbf{R})$, and $E_{m-1}^{\text{ref}}(\mathbf{R})$, and a single correlated energy $E_{m+1}(\mathbf{R}_e)$ calculated at the reference geometry \mathbf{R}_e . In fact, eq 3 is the simplest expression that one can propose to extrapolate the energy based on scaling the correlation energy or the part of it from basis set m to basis $m + 1$. Note that this extrapolation scheme is analytic, resulting in a smooth PES. Indeed, it can be used for calculating enough information about the PES such

that it may be fitted to some functional form for use in dynamics calculations. Indeed, one may even envision the development of analytic gradients for the energy resulting from eq 3 that could be exploited in direct dynamics calculations.⁶³ Various choices have been utilized for the reference energy along the test PES cut mentioned above. The calculated raw VTZ and CS VQZ energies were then used to obtain the extrapolated correlation energy at the limit of an infinite basis set, by employing the uniform singlet- and triplet-pair extrapolation (USTE) method,⁶⁵

$$E_X^{\text{cor}} = E_{\infty}^{\text{cor}} + \frac{A_3}{(X + \alpha)^3} + \frac{A_5}{(X + \alpha)^5} \quad (6)$$

where

$$A_5 = A_5(0) + cA_3^n \quad (7)$$

with $A_5(0)$ being the basis-set error in the energy for a pure pair–triplet interaction, and c and n extra universal parameters for a chosen level of theory. Note that this protocol has only two parameters, E_{∞}^{cor} and A_3 , which are to be determined from the actual calculated raw VTZ and CS VQZ correlation energies, thence with distinct T and Q cardinal numbers. Because the USTE method has been shown to provide good theoretical results,^{65–70} even when extrapolated from a pair of cardinal numbers as low as (D, T) , the second step consisted of comparing the above results with the correlation energies that are obtained via direct CBS extrapolation of the calculated raw VDZ and VTZ correlation energies. Such a comparison led to interaction correlation energies that differ in no case by more than 1.2 kcal mol^{−1} from the (T, Q) ones above obtained, with a root mean squared deviation of $\text{rmsd} = 0.5$ kcal mol^{−1} over the 30 calculated test points. Specifically, for the innermost 4 points ($r_2 \leq 3.25a_0$), $\text{rmsd} = 0.7$ kcal mol^{−1}, while for the outer 26 points, $\text{rmsd} = 0.5$ kcal mol^{−1}. Given the relatively modest accuracy of our MRCI calculations, we have chosen for simplicity the direct CBS(D, T) extrapolation scheme.

We now address the CBS extrapolation of the CASSCF part of the energy. The only two-point extrapolation formulas that are available are for the Hartree–Fock energy, as suggested by Jensen⁷¹ and re-examined by Karton and Martin.⁷² However, such protocols employ only basis where the lowest pair of cardinal numbers is (T, Q) , namely $E_X^{\text{ref}} = E_{\infty}^{\text{ref}} + AX^{-5.34}$, which the authors claim to show a respectable accuracy of $\lesssim 0.12$ kcal mol^{−1}.⁷² Such a formula has been postulated by one of us⁶⁵ to be applicable also to the CASSCF energy in MRCI calculations and tested with good results. Can such a formula be useful for extrapolations of (D, T) CASSCF energies? Of course, there is no reason for principle to expect it to be valid in such a case, although the somewhat smaller accuracy requested for the CBS target energy may well justify a trial. For this purpose, we have utilized the same set of test geometries considered above for the correlation energy. First, we have carried out CBS extrapolations of the calculated raw CASSCF/VTZ and CASSCF/VQZ energies and then performed corresponding CBS extrapolations but using the CASSCF energies only for the (D, T) pair. Interestingly, the resulting interaction CBS/CASSCF energies have shown in this case too a satisfactory accord with each other, namely a rmsd of 1.4 kcal mol^{−1} and 0.09 kcal mol^{−1} in the interaction CBS/CASSCF energies for the above inner and outer parts of the chosen PES cut. On the basis of this, and reiterating the non-negligible errors that are expected from the raw ab initio calculations themselves, we

have chosen the direct CBS(D,T) extrapolation by simply using the formula proposed by Karton and Martin for the (T , Q) cardinal number pair.

3. DMBE POTENTIAL ENERGY SURFACE FOR ClO₂

In accordance with the DMBE method,^{57–60} the PES of ClO₂ assumes the form

$$V(\mathbf{R}) = \sum_{i=1}^3 V_i^{(2)}(R_i) + V_{\text{EHF}}^{(3)}(\mathbf{R}) + V_{\text{dc}}^{(3)}(\mathbf{R}) + V_{\text{elec}}^{(3)}(\mathbf{R}) \quad (8)$$

where $V_i^{(2)}(R_i)$ represents the two-body energy terms, $V_{\text{EHF}}^{(3)}(\mathbf{R})$ the three-body extended Hartree–Fock (EHF) energy, $V_{\text{dc}}^{(3)}(\mathbf{R})$ the three-body dynamical correlation energy, and $V_{\text{elec}}^{(3)}(\mathbf{R})$ the three-body electrostatic energy.

3.1. Two-Body Terms. The diatomic potential curves have been modeled using the Extended Hartree–Fock Approximate Correlation Energy model for 2-body interactions with inclusion of the united atom limit⁷³(EHFACE2U), with the available parameters being determined by fitting experimental and ab initio data. Thus, it assumes the general form^{58,73}

$$V^{(2)}(R) = V_{\text{EHF}}^{(2)}(R) + V_{\text{dc}}^{(2)}(R) \quad (9)$$

where the EHF label refers to the extended Hartree–Fock type energy and dc labels the dynamical correlation energy. As usual, the latter is modeled semiempirically as⁷⁴

$$V_{\text{dc}}^{(2)}(R) = - \sum_{n=6,8,10} \chi_n(R) C_n R^{-n} \quad (10)$$

where the C_n values have been taken from ref 75 for O₂ and ref 76 for ClO, with the damping function for the dispersion coefficients assuming the form

$$\chi_n(R) = \left[1 - \exp\left(-A_n \frac{R}{\rho} - B_n \frac{R^2}{\rho^2}\right) \right]^n \quad (11)$$

In eq 11, A_n and B_n are auxiliary functions that are defined by

$$A_n = \alpha_0 n^{-\alpha_1} \quad (12)$$

$$B_n = \beta_0 \exp(-\beta_1 n) \quad (13)$$

where α_0 , β_0 , α_1 , and β_1 are universal dimensionless parameters for all isotropic interactions:^{57,58} $\alpha_0 = 16.36606$, $\alpha_1 = 0.70172$, $\beta_0 = 17.19338$, and $\beta_1 = 0.09574$. In turn, the scaling parameter ρ is defined as

$$\rho = 5.5 + 1.25R_0 \quad (14)$$

where $R_0 = 2(\langle r_A^2 \rangle^{1/2} + \langle r_B^2 \rangle^{1/2})$ is the Le Roy⁷⁷ parameter for onset of the undamped R^{-n} expansion, and $\langle r_X^2 \rangle$ is the expectation value of the squared radius for the outermost electrons of atom X (where X = A and B). Finally, the exponential decaying portion of the EHF-type energy term assumes the general form

$$V_{\text{EHF}}^{(2)}(R) = -\frac{D}{R} \left(1 + \sum_{i=1}^n a_i r^i \right) \exp(-\gamma r) \quad (15)$$

where

$$\gamma = \gamma_0 [1 + \gamma_1 \tanh(\gamma_2 r)] \quad (16)$$

In eq 16, $r = R - R_e$ is the displacement from the equilibrium diatomic geometry, and D and a_i ($i = 1, \dots, n$) are adjustable

parameters to be fitted to the respective asymptotic calculations described in Section Computational Details. Figure 2 (panels a–d) show the final asymptotic curves, and Table 1 summarizes their respective numerical values.

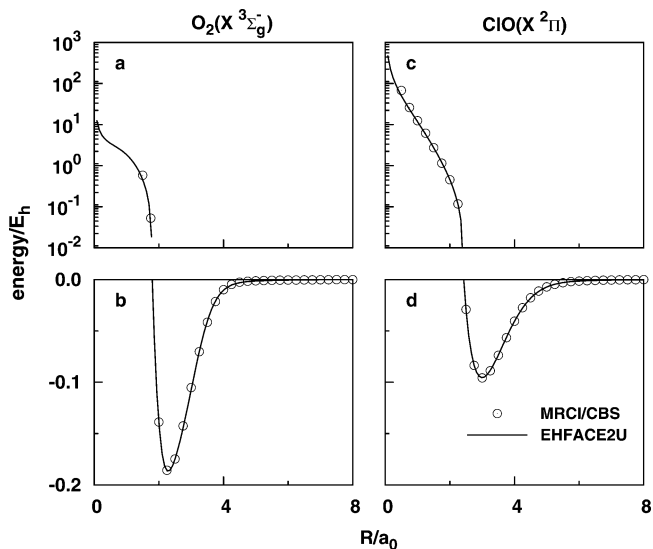


Figure 2. EHFACE2U energy curves for O₂(X³Σ_g[−]) and ClO(X²Π) and fitted CBS(D,T)/MRCI/cc-pVXZ ab initio calculations. Key as in (d).

Table 1. Parameters in the Two-Body Energy Curves

	O ₂ (X ³ Σ _g [−])	ClO(X ² Π)
$R_e(a_0)$	2.280 00	3.000 00
$D(E_h)$	0.372 88	0.227 82
$a_1(a_0^{-1})$	1.919 28	2.447 09
$a_2(a_0^{-2})$	0.657 01	1.291 77
$a_3(a_0^{-3})$	2.856 00	0.792 80
$\gamma_0(a_0^{-1})$	1.337 61	1.898 13
$\gamma_1(a_0^{-1})$	3.347 21	2.258 89
$\gamma_2(a_0^{-1})$	0.276 32	0.086 51
$R_0(a_0)$	5.661 60	6.8402
$C_6/(E_h a_0^{-6})$	15.40 ^a	38.67 ^b
$C_8/(E_h a_0^{-8})$	235.22 ^a	747.10 ^b
$C_{10}/(E_h a_0^{-10})$	4066.24 ^a	18908.15 ^b

^aFrom ref 75. ^bFrom ref 76.

3.2. Three-Body Dynamical Correlation Energy. The three-body dynamical correlation energy can be calculated from dispersion coefficients for the different atom–diatom subsystems. The analytical expression for this energy assumes the form

$$V_{\text{dc}}^{(3)}(\mathbf{R}) = \sum_{i=1}^3 \sum_n f_i(\mathbf{R}) \chi_n(r_i) C_n^{(i)}(R_i, \theta_i) r_i^{-n} \quad (17)$$

where the i label represents the I–JK channel associated with the center of mass separation r_i ; R_i is the J–K bond distance, and $\cos \theta_i = \vec{r}_i \cdot \vec{R}_i / r_i R_i$. (For the notation see Figure 1 of ref S9.) The function $f(\mathbf{R})$ is a switching function, where the value must be +1 at $R_i = R_i^e$ and $r_i \rightarrow \infty$ and 0 when $R_i \rightarrow \infty$. One such form is⁷⁸

$$f_i = \frac{1}{2} \{ 1 - \tanh[\xi(\eta s_i - s_j - s_k)] \} \quad (18)$$

Table 2. Numerical Values, In Atomic Units, of the Parameters in eq 20

	$C_6^0(R)$	$C_6^2(R)$	$C_8^0(R)$	$C_8^2(R)$	$C_8^4(R)$	$C_{10}^0(R)$
Cl–O ₂						
$R_M(a_0)$	3.600	3.2413	3.5830	3.2634	3.2160	3.5725
$D_M(E_h)$	101.1159	17.5016	1878.3501	1191.1442	129.1260	45720.1328
$a_1(a_0^{-1})$	1.36 247 475	1.19 866 305	1.25 234 783	1.22 650 815	1.69 115 168	1.17 982 007
$a_2(a_0^{-2})$	0.46 790 825	0.39 489 092	0.42 930 969	0.40 008 804	0.90 531 324	0.37 970 240
$a_3(a_0^{-3})$	3.248×10^{-5}	-1.8353×10^{-3}	3.7966×10^{-3}	-7.6684×10^{-3}	0.01 438 659	-4.7387×10^{-3}
$b_2(a_0^{-2})$	0.41 537 660	0.52 088 304	0.32 308 184	0.55 911 294	1.15 737 628	0.27 539 940
$b_3(a_0^{-3})$	4.08×10^{-2}	3.91×10^{-2}	3.41×10^{-2}	6.78×10^{-2}	0.25 045 127	3.48×10^{-2}
O–ClO						
$R_M(a_0)$	4.000	3.7954	3.9707	3.7956	3.7863	3.9492
$D_M(E_h)$	118.8870	12.9316	2663.3808	901.3798	56.5747	81258.9295
$a_1(a_0^{-1})$	1.29 474 724	1.06 932 476	1.19 014 550	1.20 944 055	1.02 064 366	1.03 818 961
$a_2(a_0^{-2})$	0.26 454 128	1.24 829 673	0.24 489 658	0.45 372 387	0.35 716 277	0.14 679 120
$a_3(a_0^{-3})$	-3.94×10^{-2}	0.53 693 123	-2.45×10^{-2}	5.29×10^{-2}	4.12 759 363	$-3.62 431 434$
$b_2(a_0^{-2})$	7.49×10^{-3}	0.94 039 970	$-0.11 394 880$	0.13 792 835	0.86 895 371	$-0.21 056 690$
$b_3(a_0^{-3})$	5.54×10^{-9}	9.99×10^{-8}	3.79×10^{-3}	6.41×10^{-2}	0.23 910 851	1.40×10^{-2}

where $s_i = R_i - R_i^c$ (corresponding expressions apply for s_j , s_k , f_j , and f_k), and η and ξ are constants chosen in order to ensure the proper asymptotic behavior. In this work we have adopted $\xi = 1.0$ and $\eta = 5.0a_0^{-1}$. Additionally, $\chi_n(r_i)$ is a damping function assuming the form shown in eq 11 with R replaced by the center-of-mass separation for the relevant atom–diatom channel and ρ chosen as the average of the respective Le Roy parameters. Finally, in eq 17, the functions $C_n^{(i)}(R_i, \theta_i)$ are the atom–diatom dispersion coefficients, which assume the form

$$C_n^{(i)}(R_i, \theta_i) = \sum_L C_n^L(R_i) P_L(\cos \theta_i) \quad (19)$$

where $P_L(\cos \theta_i)$ denotes the L th term of the Legendre polynomial expansion. In the summation in eq 19, only the $L = 0, 2$, and 4 components have been considered, with the involved internuclear dependence being estimated as reported elsewhere⁷⁹ (i.e., using the dipolar polarizabilities calculated in the present work at the MRCI/cc-pVQZ level of theory together with the generalized Slater–Kirkwood approximation).⁸⁰ Atom–diatom dispersion coefficients were then fitted to the form

$$C_n^{A-BC}(R) = C_n^{AB} + C_n^{AC} + D_M(1 + \sum_{i=1}^3 a_i r^i) \exp(-a_1 r) - \sum_{i=2}^3 b_i r^i \quad (20)$$

where $r = R - R_M$ is the displacement relative to the position of the maximum. The parameters that resulted from such fitting are reported in Table 2, whereas the internuclear dependence of the dispersion coefficients is shown in Figure 3 (panels a–f).

As noted elsewhere,⁷⁸ eq 17 causes an overestimation of the dynamical correlation energy at the atom–diatom dissociation channels. In order to correct such a behavior, we have multiplied the two-body dynamical correlation energy for the i th pair by $f_i(\mathbf{R})$ and, correspondingly, for channels j and k . This ensures⁷⁸ that the only two-body contribution at the i th channel is that of JK.

3.3. Electrostatic Energy. The electrostatic energy potential terms of the ClO₂ system have their origin in the interaction of the quadrupole moment of the oxygen atom with

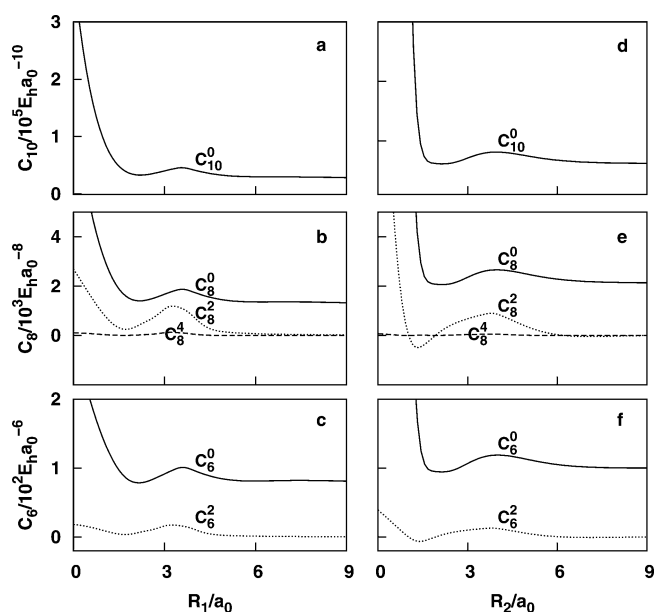


Figure 3. Dispersion coefficients for atom–diatom asymptotic channels of ClO₂ as a function of the corresponding atom–diatom separation.

the dipole and quadrupole moments of ClO and to the interaction of the chlorine atom quadrupole with the O₂ quadrupole. Similarly to its treatment in eq 17, the electrostatic energy of the ClO₂ molecule can be approximated by

$$V_{\text{elec}}^{(3)}(\mathbf{R}) = \sum_{i=1}^3 f_i(\mathbf{R}) C_4(R_i, r_i) \mathcal{A}_{\text{DQ}}(\theta_{a,i}, \gamma_i, \phi_{ab,i}) r_i^{-4} + C_5(R_i, r_i) \mathcal{A}_{\text{QQ}}(\theta_{a,i}, \gamma_i, \phi_{ab,i}) r_i^{-5} \quad (21)$$

where $i, f_i(\mathbf{R}), R_i, r_i$, and γ_i have the same meaning as above, $\theta_{a,i}$ is the angle that defines the atomic quadrupole orientation, and $\phi_{ab,i}$ is the corresponding dihedral angle. The coefficients $C_4(R_i, r_i)$ and $C_5(R_i, r_i)$ for the i th channel A–BC, are given by

$$C_4(R_i, r_i) = \frac{3}{2} Q_A D_{BC}(R_i) \chi_4(r_i)$$

$$C_5(R_i, r_i) = \frac{3}{2} Q_A Q_{BC}(R_i) \chi_5(r_i) \quad (22)$$

where $\chi_4(r_i)$ and $\chi_5(r_i)$ are convenient damping functions of the type given by eq 11. $D_{BC}(R_i)$ is the diatomic electric dipole moment, $Q_{BC}(R_i)$ is the corresponding diatomic electric quadrupole moment, and Q_A is the quadrupole moment of atom A. In this work, we have calculated at the MRCI/cc-pVQZ level of theory the value $Q_{Cl(^2P)} = 1.55628ea_0^2$ and used the value $Q_{O(^3P)} = -0.92008ea_0^2$ obtained elsewhere.⁸¹ Notice also that the dipole–quadrupole term $C_4(R_i, r_i)$ for Cl–O₂ will be absent from the $V_{elec}^{(3)}(\mathbf{R})$ expansion in eq 21 because O₂ has no dipole moment. The angular variations of \mathcal{A}_{DQ} and \mathcal{A}_{QQ} are defined by⁸²

$$\mathcal{A}_{DQ}(\theta_a, \gamma, \phi_{ab}) = \cos \gamma (3 \cos^2 \theta_a - 1) + 2 \sin \theta_a \sin \gamma \cos \theta_a \cos \gamma \cos \phi_{ab} \quad (23)$$

and

$$\mathcal{A}_{QQ}(\theta_a, \gamma, \phi_{ab}) = 1 - 5 \cos^2 \theta_a - 5 \cos^2 \gamma + 17 \cos^2 \theta_a \cos^2 \gamma + 2 \sin^2 \theta_a \sin^2 \gamma \cos^2 \phi_{ab} + 16 \sin \theta_a \sin \gamma \cos \theta_a \cos \gamma \cos \phi_{ab} \quad (24)$$

To eliminate the angle θ_a in eqs 23 and 24, we use the classical optimized-quadrupole (COQ) model,^{79,83–85} obtaining⁸⁶

$$\theta_a = \mp \arctan \{ 2 \sin \gamma (8C_5 \cos \gamma + C_4 R) / [256C_5^2 \sin^2 \gamma \cos^2 \gamma + 2C_4 C_5 R \cos \gamma (36 - 25 \sin^2 \gamma) + 361C_5^2 \sin^4 \gamma + 9C_4^2 R^2 + 144C_5^2]^{1/2} - (5C_4^2 R^2 + 456C_5^2 \sin^2 \gamma \mp 3C_4 R \cos \gamma \pm C_5 (19 \sin^2 \gamma - 12) + \delta) \} \quad (25)$$

which is used to replace θ_a in eqs 23 and 24. A numerical parameter $\delta = 10^{-10}$ was included in this expression to prevent division by zero, and the solution corresponding to the equilibrium geometry of the diatomic molecules has been used.

In order to model the variation of the O₂ and ClO quadrupole moment and ClO dipole moment with the internuclear distance in eqs 22, we have calculated those quantities at the MRCI/cc-pVQZ level of theory as a function of the internuclear distance of the diatomic molecules. The quadrupole moment values so obtained are then fitted to the form⁸⁵

$$Q(R) = A(1 + \sum_{i=1}^3 a_i r^i) \exp(-\sum_{i=1}^3 b_i r^i) + \frac{M_6}{R^6} \chi_8(R) + Q_\infty \quad (26)$$

where $r = R - R_{ref}$ and R_{ref} is a reference distance corresponding to the maximum in the $Q(R)$ curve, while the dipole moment values obtained are fitted to⁸⁵

$$D(R) = A(1 + \sum_{i=1}^3 a_i r^i) \exp(-\sum_{i=1}^3 b_i r^i) \quad (27)$$

where $r = R - R_{ref}$ and R_{ref} is a reference distance corresponding to the maximum in the $D(R)$ curve. All the fitted parameters in eqs 26 and 27 are given in Table 3, while a graphical view of the functions is shown in panels a to c of Figure 4.

Table 3. Numerical Values of the Parameters in Eqs 26 and 27

	$Q_{O_2}(R)$	$Q_{ClO}(R)$	$D_{ClO}(R)$
$Q_\infty/e a_0^2$	0.919 00	2.049 65	–
$M_6/e a_0^2$	1946.13	9413.93	–
R_{ref}/a_0	3.8117	9.459 86	3.6927
A/e_0	−0.094 23	6.2×10^{-12}	−0.194 00
a_1/a_0^{-1}	−0.194 01	5.451 92	0.970 09
a_2/a_0^{-2}	2.8671	−2.616 55	0.222 51
a_3/a_0^{-3}	−0.340 79	0.199 27	7.7×10^{-12}
b_1/a_0^{-1}	1.378 45	6.167 98	2.550 49
b_2/a_0^{-2}	0.898 98	0.440 84	0.273 20
b_3/a_0^{-3}	0.151 72	0.0	0.001

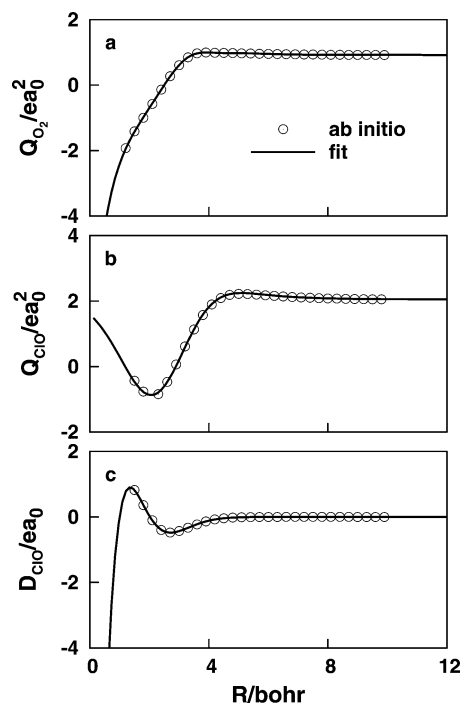


Figure 4. Dipole and quadrupole permanent electrostatic moments as a function of internuclear distance. In all panels, open circles represent the electrostatic moments calculated ab initio at the MRCI/AVQZ level of theory. Solid lines in panels a and b represent the fit of eq 26 to the quadrupole moments of O₂(X³Σ_g[−]) and ClO(X²Π), respectively, and in panel c the solid line represents the fit of eq 27 to the dipole moment of ClO(X²Π).

3.4. Three-Body Extended Hartree–Fock Energy Term. To obtain the EHF energy contribution, we first subtract from the CBS(D,T)/MRCI/cc-pVXZ energies the two-body, three-body dynamical correlation and the three-body electrostatic contributions obtained in Two-Body Terms, Three-Body Dynamical Correlation Energy, and Electrostatic Energy, respectively. The data so obtained is then modeled with the following three-body distributed polynomial⁸⁷ form

$$V_{\text{EHF}}^{(3)}(\mathbf{R}) = \sum_{\alpha=1}^n P_{\alpha}(R_1, R_2, R_3) \prod_{i=1}^3 \{1 - \tanh[\gamma_{i,\alpha}(R_i - R_{i,\alpha}^{\text{ref}})]\} \quad (28)$$

where $P_{\alpha}(R_1, R_2, R_3)$ is the α th polynomial. Up to the 6th order, it assumes the form

$$\begin{aligned} P_{\alpha}(R_1, R_2, R_3) = & c_1 + c_2 Q_1 + c_3 Q_3 + c_4 Q_1^2 + c_5 S_{2a}^2 \\ & + c_6 Q_1 Q_3 + c_7 S_{2b}^2 + c_8 Q_1^3 + c_9 Q_1 S_{2a}^2 + c_{10} S_3^3 \\ & + c_{11} Q_1^2 Q_3 + c_{12} Q_1 S_{2b}^2 + c_{13} Q_3 S_{2a}^2 + c_{14} Q_1^4 + c_{15} Q_1^2 S_{2a}^2 \\ & + c_{16} S_{2a}^4 + c_{17} Q_1 S_3^3 + c_{18} Q_1^3 Q_3 + c_{19} Q_1^2 S_{2b}^2 \\ & + c_{20} Q_1 Q_3 S_{2a}^2 + c_{21} Q_3 S_3^3 + c_{22} S_{2a}^2 S_{2b}^2 + c_{23} Q_1^5 \\ & + c_{24} Q_1^3 S_{2a}^2 + c_{25} Q_1 S_{2a}^4 + c_{26} Q_1^2 S_3^3 + c_{27} S_{2a}^2 S_3^3 \\ & + c_{28} Q_1^4 Q_3 + c_{29} Q_1^3 S_{2b}^2 + c_{30} Q_1^2 Q_3 S_{2a}^2 + c_{31} Q_1 Q_3 S_3^3 \\ & + c_{32} Q_1 S_{2a}^2 S_{2b}^2 + c_{33} Q_3 S_{2a}^4 + c_{34} S_{2b}^2 S_3^3 + c_{35} Q_1^6 \\ & + c_{36} Q_1^4 S_{2a}^2 + c_{37} Q_1^2 S_{2a}^4 + c_{38} Q_1^3 S_3^3 + c_{39} Q_1 S_{2a}^2 S_3^3 \\ & + c_{40} S_{2a}^6 + c_{41} S_3^6 + c_{42} Q_1^5 Q_3 + c_{43} Q_1^4 S_{2b}^2 + c_{44} Q_1^3 Q_3 S_{2a}^2 \\ & + c_{45} Q_1^2 Q_3 S_3^3 + c_{46} Q_1^2 S_{2a}^2 S_{2b}^2 + c_{47} Q_1 Q_3 S_{2a}^4 \\ & + c_{48} Q_1 S_{2b}^2 S_3^3 + c_{49} Q_3 S_{2a}^2 S_3^3 + c_{50} S_{2a}^4 S_{2b}^2 \end{aligned} \quad (29)$$

where $S_{2a}^2 = Q_2^2 + Q_5^2$, $S_{2b}^2 = Q_2^2 - Q_5^2$, and $S_3^3 = Q_3^3 - 3Q_2^2 Q_3$, with Q_i ($i = 1 - n$) are symmetry coordinates that are defined for the α th polynomial by

$$\begin{pmatrix} Q_{1,\alpha} \\ Q_{2,\alpha} \\ Q_{3,\alpha} \end{pmatrix} = \begin{pmatrix} \sqrt{\frac{1}{3}} & \sqrt{\frac{1}{3}} & \sqrt{\frac{1}{3}} \\ 0 & \sqrt{\frac{1}{2}} & -\sqrt{\frac{1}{2}} \\ \sqrt{\frac{2}{3}} & -\sqrt{\frac{1}{6}} & -\sqrt{\frac{1}{6}} \end{pmatrix} \begin{pmatrix} R_1 - R_{1,\alpha}^{\text{ref}} \\ R_2 - R_{2,\alpha}^{\text{ref}} \\ R_3 - R_{3,\alpha}^{\text{ref}} \end{pmatrix} \quad (30)$$

Note that in eq 29 the α subscript has been omitted from the $c_{i,\alpha}$ linear coefficients and $Q_{i,\alpha}$ symmetry coordinates for simplicity. To model $V_{\text{EHF}}^{(3)}$ in eq 28, we have started as usual by choosing convenient geometries where to center a given set of polynomials. Those were then calibrated via $\gamma_{i,\alpha}$ and $c_{i,\alpha}$ in eqs 28 and 29, respectively, with the quality of the resulting least-squares fit determining the addition of further polynomials. The final set of values for all parameters in eqs 28 and 29 are given in Tables S1, S2, S3, and S4 of the Supporting Information with the final stratified rmsd displayed in Table 4.

4. MAIN FEATURES OF THE POTENTIAL ENERGY SURFACE

Figures 5 (panels a and b) and 6 (panels a and b) depict the final fit, and Table 5 gathers the attributes of the resulting PES, hereafter denoted as DMBE PES. The DFT calculations of Zhu and Lin⁴⁵ at the G2M(CC2)//PW91PW91/6-311 + G(3df) and G2M(CC5)//PW91PW91/6-311 + G(3df) levels of theory will be hereafter denoted as ZL-I PES and ZL-II PES, respectively.

Table 5 shows that the energy interval ranging from the global minimum energy of the PES to 80 kcal mol⁻¹ above this value comprises all relevant stationary states, as well as both Cl–O₂ and O–ClO atom–diatom channels. This region is

Table 4. Stratified Root-Mean-Square Deviations^a

energy ^b	no. of points	maximum deviation	rmsd
10	271	0.329	0.121
20	489	2.068	0.412
30	575	2.855	0.611
40	757	2.855	0.605
50	850	4.612	0.704
60	993	4.612	0.804
70	1373	4.612	0.804
80	2044	4.612	0.758
90	2203	4.612	0.807
100	2293	6.122	0.864
200	3067	6.717	1.038
300	3114	6.717	1.060
400	3152	6.717	1.087
500	3214	6.717	1.113
1000	3223	6.717	1.121

^aEnergy, maximum deviation, and rmsd in kcal mol⁻¹. ^bRelative to the global minimum.

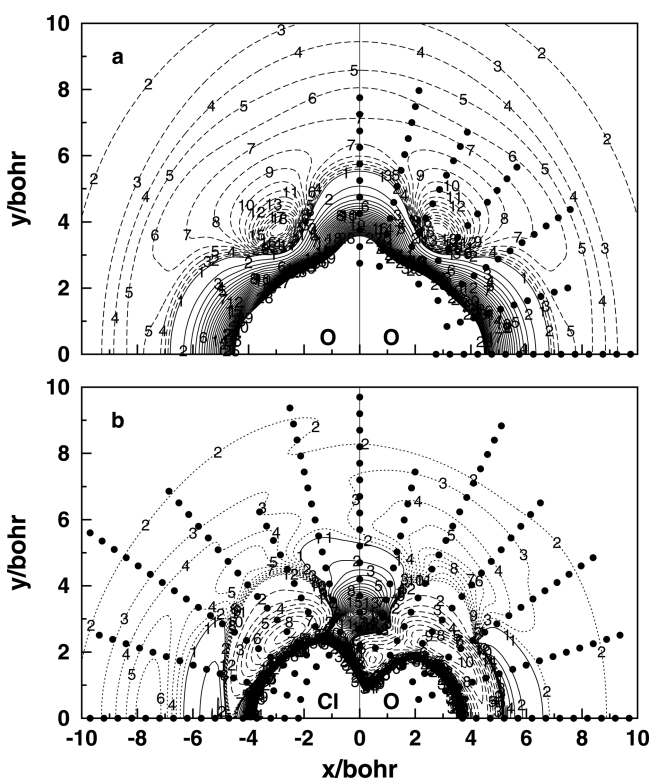


Figure 5. Isoenergy relaxed contour plots. The solid black dots indicate the ab initio points used for the fit. Keys for the energy of the first contour (E_0/E_h) and energy intervals ($\Delta E/E_h$): (a) $E_0/E_h = -0.18648764$; solid lines, $\Delta E/E_h = 0.003$; dashed lines, $\Delta E/E_h = -0.0003$; (b) $E_0/E_h = -0.09545844$; solid lines, $\Delta E/E_h = 0.003$; dashed lines, $\Delta E/E_h = -0.01$; dotted lines, $\Delta E/E_h = -0.0003$. The intervals of relaxation are $2.1 \leq R_1/a_0 \leq 2.4$ for the Cl–O₂ channel shown in panel a and $2.7 \leq R_2/a_0 \leq 4.3$ for the O–ClO channel shown in panel b.

mapped by over 2000 geometry points, which are modeled by the DMBE PES within a rmsd below 0.804 kcal mol⁻¹, as shown in Table 4. The set of calculations employed is completed by another 1200 geometry points, covering up to 1000 kcal mol⁻¹ above the global minimum and modeled by the DMBE PES within a rmsd below 1.13 kcal mol⁻¹.

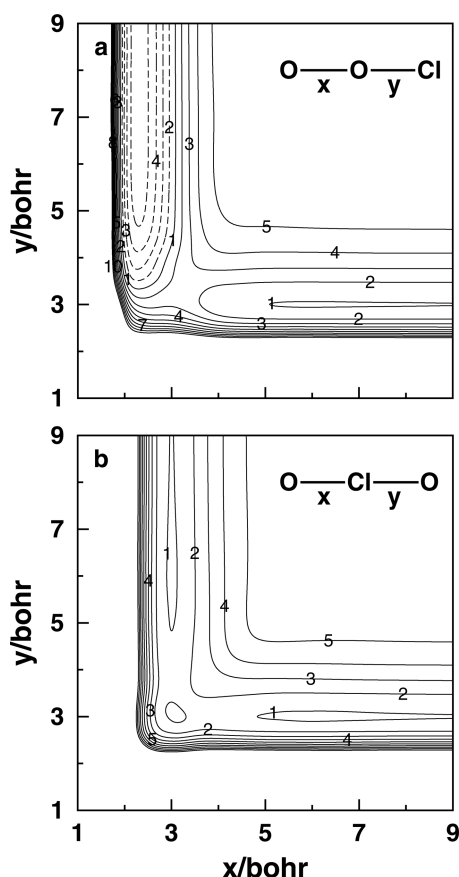


Figure 6. Isoenergy linear contour plots. All contours start at $E_0/E_h c = -0.095458441$. Energy intervals: solid lines, $\Delta E/E_h = 0.02$; dashed lines, $\Delta E/E_h = -0.02$.

The global minimum of the DMBE PES is the ClOO structure, located energetically $120.8 \text{ kcal mol}^{-1}$ below atomization and $3.7 \text{ kcal mol}^{-1}$ below the $\text{Cl} + \text{O}_2$ dissociation channel. This last value shows a discrepancy of $0.99 \text{ kcal mol}^{-1}$ with respect to the experimental measurements of Suma et al.,⁴⁸ which is expected to increase up to $\approx 1.99 \text{ kcal mol}^{-1}$ with the inclusion of spin-orbit effects.⁴⁷ However, as shown elsewhere,⁴⁷ only within a multiconfigurational approach with larger active spaces, including most of the inner core electrons, and using basis sets containing large sets of diffuse functions such as the AVXZ one, could such a difference be overcome, thence raising the cost of the calculations beyond affordability in the context of the present work. A similar reasoning applies to the Cl–O bond distance, which is predicted by the DMBE PES to be $\approx 0.2128a_0$ larger than the experimental value. Indeed, geometry optimizations of the ClOO global minimum at the MRCI/VDZ and MRCI/VTZ levels of theory yielded for the Cl–O bond distance values of $4.656a_0$ and $4.1840a_0$ in the same order, thence in general agreement with the CBS(D, T)/MRCI + Q/cc-pVXZ-based DMBE PES value of $4.1510a_0$.

The OCIO T-shaped minimum is the next species in energy, lying $8.1 \text{ kcal mol}^{-1}$ above the ClOO minimum. The same trend has been found in both ZL-I and ZL-II PESs, with the OCIO structure lying $2.4 \text{ kcal mol}^{-1}$ above the ClOO global minimum in the ZL-I PES and $0.8 \text{ kcal mol}^{-1}$ in the ZL-II PES. An inverse trend has been reported by Karton et. al.⁴¹ using the W4 protocol.^{50–53} In their calculations, the OCIO structure is more stable by $0.45 \text{ kcal mol}^{-1}$. The ordering as given by the DMBE PES is kept when we add the appropriate ZPE

corrections calculated from our normal-mode frequencies in Table 5. In fact, the energy difference between the ClOO global minimum and the OCIO structure increases, now lying $8.68 \text{ kcal mol}^{-1}$ above ClOO.

Zhu and Lin⁴⁵ reported two first-order transition states, TS1 and TS2, related to the ClOO and OCIO structures. In the ZL-I PES, the TS1 lies $65.7 \text{ kcal mol}^{-1}$ above the global minimum and works as a barrier for the $\text{ClOO} \rightleftharpoons \text{OCIO}$ transition. In turn, TS2 lies $63.9 \text{ kcal mol}^{-1}$ above the global minimum in the ZL-I PES, functioning as a barrier for the $\text{OCIO}' \rightleftharpoons \text{O}'\text{ClO}$ isomerization. Energetically, besides the significant height of the barriers that both TS1 and TS2 represent, they lie above the $\text{O} + \text{ClO}$ dissociation by $5.3 \text{ kcal mol}^{-1}$ and $3.5 \text{ kcal mol}^{-1}$, respectively. In our calculations, we have not found the corresponding structures. As shown in Table 5, all stationary states encountered in the DMBE PES lie below the $\text{O} + \text{ClO}$ dissociation and occur near the $\text{O} - \text{ClO}$ dissociation channel. This suggests that in the DMBE PES, the ClOO and OCIO species as well as the OCIO' and O'ClO isomers can only be connected through the $\text{O} + \text{ClO}$ dissociation channel.

Figure 5 (panels a and b) shows a (x, y) representation of relaxed contour plots of the DMBE PES for $\text{Cl}-\text{O}_2$ and $\text{O}-\text{ClO}$ interactions, respectively. Panel a reveals a strictly attractive long-range form for both C_{2v} and $\text{Cl}-\text{OO}$ linear insertions up to $r_1 \approx 6.0a_0$. In this region, we observe a small barrier of $\approx 0.18 \text{ kcal mol}^{-1}$ for linear insertion lying $\approx 0.94 \text{ kcal mol}^{-1}$ below $\text{Cl} + \text{O}_2$ dissociation, and also a small barrier for C_{2v} insertion of $\approx 0.18 \text{ kcal mol}^{-1}$ lying below $\text{Cl} + \text{O}_2$ dissociation by $\approx 1.1 \text{ kcal mol}^{-1}$. The latter corresponds to the first-order transition state LRTS4 with properties shown in Table 5. However, the most prominent aspect of panel a appears for shorter r_1 values, and given the optimization range used to generate panel a, we can safely say that it corresponds to the ClOO global minimum in the form of the two symmetric isomers visible in Figure 5. It is interesting to note that LRTS4 acts as an $\text{ClO}'\text{O} \rightleftharpoons \text{ClOO}'$ isomerization barrier. For other insertions, panel a shows a strictly repulsive topology, without revealing any path connecting the ClOO structure with other regions of the DMBE PES. Note that the OCIO symmetric species is absent from panel a due to the optimization range of the R_1 coordinate.

Panel b reveals a sophisticated topology for $\text{O}-\text{ClO}$ interactions, in agreement with the five long-range stationary states shown in Table 5. For linear $\text{O}-\text{ClO}$ insertions ($\gamma_2 = 180$ deg and $\alpha_2 = 0$ deg), we first see a linear minimum of $\approx 1.0 \text{ kcal mol}^{-1}$ below $\text{O} + \text{ClO}$ dissociation, followed by a barrier of $\approx 3.8 \text{ kcal mol}^{-1}$ above $\text{O} + \text{ClO}$ dissociation. For shorter values of r_2 , we see a OCIO linear first-order transition state (LRTS3) followed by a very repulsive part of the DMBE PES. As the α_2 angle increases (γ_2 decreases), a series of stationary states appears as given in Table 5, namely LRM2, LRTS2, LRTS1, and LRM1, the latter for $\gamma_2 = 0$ deg and $\alpha_1 = 180$ deg. Among those structures, only LRM2 and LRM1 may be more clearly identified in Figure 5b. The two more prominent aspects of panel b can be seen for shorter values of r_2 , namely two minima appearing in the Figure, one for $\gamma_2 > 90$ deg, the another for $\gamma_2 < 90$ deg. Given the optimization range used to generate panel b, we can safely say that for $\gamma_2 < 90$ deg, the minimum visible in the plot corresponds to the OCIO structure. LRTS2 would then function as an $\text{OCIO}' \rightleftharpoons \text{O}'\text{ClO}$ isomerization barrier, thus playing for the DMBE PES a similar role as TS2 does for ZL-I PES. Similarly, due to the optimization range used in panel b, the structure appearing for $\gamma_2 < 90$ deg can be safely

Table 5. Stationary Points of the Title System^a

R_1	R_2	α_3	$\omega_s, \omega_b, \omega_a$	energy ^b	energy ^c	energy ^d	energy ^e	level of theory
Cl + O ₂ Atom-Diatom Dissociation Energy ^f								
2.2800				−117.1	−57.2	0	3.7	DMBE
2.2819				−117.97 ± 0.05 ^g				exptl ⁵⁶
C _s Global Minimum (ClOO)								
2.2696	4.0421	115.7	1538, 403, 194			−2.46		ref 17
2.3017	3.7624	116.6	1417, 516, 297		−60.4		0.0	ZL-I
2.3168	3.8267	116.9	1379, 494, 279		−59.9		0.0	ZL-II
2.2828	3.8399	115.37		−121.88			0.45	ref 41 ^h
2.2771	3.9854	115.5	1498, 422, 203			−4.26		ref 47 ⁱ
2.2936	4.1510	114.8	1513, 381, 198	−120.8	−60.9	−3.7	0.0	DMBE
2.2809	3.9382	115.4				−4.69 ± 0.1		exptl ^{47,48}
2.3244	3.4582	110	1443, 408, 192	−122.7 ± 0.8 ^g				exptl ⁵⁶
TS1								
3.4770	3.0103	67.1			5.3		65.7	ZL-I
3.4770	3.0103	67.1			3.4		63.3	ZL-II
ClOO Linear Long-Range Minimum (LRM1)								
6.0209	2.9990	180	33, 13, 833	−60.2	−0.3	56.9	60.6	DMBE
C _s Long-Range Transition State (LRTS1)								
6.7954	3.0018	66.0	829, 48, 55i	−60.2	−0.3	56.9	60.6	DMBE
C _s Long-Range Transition State (LRTS2)								
7.1490	2.9902	38.0	48i, 93, 853	−60.8	−0.9	56.3	60.0	DMBE
C _s Long-Range Minimum (LRM2)								
7.2388	2.9925	37.8	48, 89, 852	−60.8	−0.9	56.3	60.0	DMBE
R_2	R_3	α_1	$\omega_s, \omega_b, \omega_a$	energy ^b	energy ^c	energy ^d	energy ^e	level of theory
O + ClO Atom-Diatom Dissociation Energy ^f								
3.0000				−59.9	0	57.2	60.9	DMBE
2.9663				−63.42 ± 0.05 ^g				exptl ⁵⁶
T-Shaped Minimum (OCIO)								
2.7832	2.7832	117.65	960, 456, 1128					ref 35
2.8270	2.8270	117.9	924, 443, 1070		−58.0	−2.2	2.4	ZL-I
2.8270	2.8270	117.9	924, 443, 1070		−59.1	−3.8	0.8	ZL-II
2.7836	2.7836	117.49		−122.33			0.0	ref 41 ^h
2.7955	2.7955	117.6	951, 466, 1154	−112.8	−52.9	4.3	8.1	DMBE
2.7776	2.7776	117.4						exptl ¹⁶
2.7798	2.7798	117.6	946, 448, 1110	−122.7 ± 1.9 ^g				exptl ⁵⁶
TS2								
3.4450	3.4450	48.8			3.5		63.9	ZL-I
OCIO Linear Long-Range Transition State (LRTS3)								
3.0685	3.0685	0	2694, 2065i, 3030	−62.1	−2.2	55.0	58.7	DMBE
C _{2v} Long-Range Transition State (LRTS4)								
6.8051	6.8051	19.4	1568, 38, 49i	−118.2	−58.3	−1.1	2.6	DMBE

^aDistances in bohr, angles in degrees, frequencies in inverse centimeters, and energies in kilocalories per mol. ^bRelative to atomization. ^cRelative to O–ClO asymptotic limit. ^dRelative to Cl–O₂ asymptotic limit. ^eRelative to global minimum. ^fWithout ZPE correction; since the energy of the isolated atoms is set to zero, the A + BC dissociation energy is equal to the BC diatomic well depth. ^gCalculated from the JANAF⁵⁶ values for the enthalpy of formation at 0 K.⁸⁸ ^hEnergy values obtained with the W4 protocol,^{50–53} other values obtained ab initio from the CCSD(T)/aug-cc-pV(Q + d)Z calculations. ⁱData obtained ab initio from CBS/MRCI + Q calculations.

assigned as the ClOO global minimum. Finally, the absence in panel b of any clear transition state between OCIO and ClOO structures reveals that any OCIO ⇌ ClOO transition may likely occur via large r_2 values, in agreement with our analysis of the energetics.

Figure 6 (panels a and b) shows stretching contour plots for Cl–O–O and O–Cl–O linear arrangements, respectively. In panel a, both atom–diatom dissociation channels may be clearly identified and a barrier of ≈ 50 kcal mol^{−1} for the collinear attack of O to the oxygen end of OCl identified. Such a barrier is also visible from panel b of Figure 5 for $\gamma_2 = 0$ deg.

5. CONCLUDING REMARKS

We have reported a single-sheeted DMBE PES potential energy surface for ground-state ClO₂ on the basis of a realistic representation of the long-range forces and a fitting to reliable ab initio calculations employing the CBS(D,T)/MRCI/cc-pVXZ level of theory. The DMBE PES accurately models the calculated data both in the region of the stationary states as well as in the dissociative channels. The topographical features of the new potential energy surface have been examined and compared with previous calculations for the title system.⁴⁵ In agreement with the previous results, we have found that the ClOO corresponds to the global minimum of the DMBE PES, lying 8.1 kcal mol^{−1} below the OCIO C_{2v} minimum, although

no stationary points connecting the ClOO and OCIO species are present in the DMBE PES. The DMBE potential energy surface reported in the present work might therefore become a key part of the investigation of chlorine oxides and is currently being used for dynamics studies of the $\text{Cl} + \text{O}_2 \rightarrow \text{ClO}_2 \rightarrow \text{ClO} + \text{O}$ reaction. Such results will be key in unveiling whether a closer attention to some details of the title potential energy surface may still be required. Irrespective of any eventual refinements, the present work paves the way for⁸⁸ a detailed dynamics study of any reactions that evolve on the potential energy surface of ground-state ClO_2 .

■ ASSOCIATED CONTENT

● Supporting Information

The final fitting parameters of the $V_{\text{EHF}}^{(3)}(\mathbf{R})$ function in eq (28) obtained as described in Three-Body Extended Hartree–Fock Energy Term are displayed in Tables S1, S2, S3, and S4. This material is available free of charge via the Internet at <http://pubs.acs.org>.

■ AUTHOR INFORMATION

Corresponding Author

*E-mail: varandas@uc.pt. Tel: + 351 239 835867. Fax: + 351 239 827703.

Notes

The authors declare no competing financial interest.

■ ACKNOWLEDGMENTS

This work has been supported by Ministerio de Ciencia e Innovación (MICINN), Spain (Grant N° CTQ2010-19232). The support to one of us (A.J.C.V.) by Fundação para a Ciência e a Tecnologia, Portugal, under contracts PTDC/CEQ-COM3249/2012 and PTDC/AAG-MAA/4657/2012, as well as the support to the Coimbra Chemistry Centre through the project PEst-OE/UI0313/2014 are also gratefully acknowledged. Support from the Brazilian funding agency Coordenação de Aperfeiçoamento de Nível Superior (CAPES) is further acknowledged. O.B.M.T. also thanks the University of Coimbra for various visits during the course of his studies.

■ REFERENCES

- (1) Molina, M. J.; Rowland, F. S. Stratospheric Sink for Chlorofluoromethanes: Chlorine Atom-Catalysed Destruction of Ozone. *Nature* **1974**, *249*, 810–812.
- (2) Brune, W. H.; Anderson, J. G.; Chan, K. R. In Situ Observations of ClO in the Antarctic: ER-2 Aircraft Results from 54°S to 72°S Latitude. *J. Geophys. Res.* **1989**, *94*, 16649–16663.
- (3) Rowland, F. S. Stratospheric Ozone Depletion. *Annu. Rev. Phys. Chem.* **1991**, *42*, 731–768.
- (4) Reid, P. J. Understanding The Phase-Dependent Reactivity of Chlorine Dioxide Using Resonance Raman Spectroscopy. *Acc. Chem. Res.* **2001**, *34*, 691–698.
- (5) Wayne, R. P. *Chemistry Of Atmospheres*; Clarendon: Oxford, 1991.
- (6) Molina, L. T.; Molina, M. J. Production of Chlorine Oxide (Cl_2O_2) from the Self-Reaction of the Chlorine Oxide (ClO) Radical. *J. Phys. Chem.* **1987**, *91*, 433–436.
- (7) Sander, S. P.; Friedl, R. R.; Yung, Y. L. Rate of Formation of the ClO Dimer in the Polar Stratosphere: Implications for Ozone Loss. *Science* **1989**, *245*, 1095–1098.
- (8) McElroy, M. B.; Salawitch, R. J.; Wofsy, S. C.; Logan, J. A. Reductions of Antarctic Ozone due to Synergistic Interactions of Chlorine and Bromine. *Nature* **1986**, *321*, 759–762.
- (9) Gole, J. L. Photochemical Isomerization Of Chlorine Dioxide and the Low-Lying Electronic State of the Asymmetric Isomer. Possible Implications for Matrix Isolation Spectroscopy. *J. Phys. Chem.* **1980**, *84*, 1333–1340.
- (10) Vaida, V.; Solomon, S.; Richard, E. C.; Ruhl, E.; Jefferson, A. Photoisomerization of OCIO: A Possible Mechanism for Polar Ozone Depletion. *Nature* **1989**, *342*, 405–408.
- (11) Curl, R. F., Jr.; Kinsey, J. L.; Baker, J. G.; Baird, J. C.; Bird, G. R.; Heiderberg, R. F.; Sugden, T. M.; Jenkins, D. R.; Kenney, C. N. Microwave Spectrum of chlorine Dioxide. I. Rotational Assignment. *Phys. Rev.* **1961**, *121*, 1119–1123.
- (12) Curl, R. F., Jr.; Heiderberg, R. F.; Kinsey, J. L. Microwave Spectrum of Chlorine Dioxide. II. Analysis of Hyperfine Structure and the Spectrum of $\text{Cl}^{35}\text{O}^{16}\text{O}^{18}$. *Phys. Rev.* **1962**, *125*, 1993–1999.
- (13) Tolles, W. M.; Kinsey, J. L.; Curl, R. F., Jr.; Heiderberg, R. F. Microwave Spectrum of Chlorine Dioxide. V. The Stark and Zeeman Effects. *J. Chem. Phys.* **1962**, *37*, 927–930.
- (14) Krishna Pillai, M. G.; Curl, R. F., Jr. Microwave Spectrum of Chlorine Dioxide. IV. Determination of Centrifugal Distortion Effects and Potential Constants. *J. Chem. Phys.* **1962**, *37*, 2921–2926.
- (15) Mariella, R. P.; Curl, R. F., Jr. Microwave Spectrum of Chlorine Dioxide. VI. $v_2 = 1$ State. *J. Chem. Phys.* **1970**, *52*, 757–763.
- (16) Miyasaka, K.; Tanoura, M.; Tanaka, K.; Tanaka, T. Microwave Spectrum of Chlorine Dioxide in Excited Vibrational States. *J. Mol. Spectrosc.* **1986**, *116*, 435–449.
- (17) Peterson, K. A.; Werner, H. J. Multireference Configuration Interaction Calculations of the Low-Lying Electronic States of ClO_2 . *J. Chem. Phys.* **1992**, *96*, 8948–8961.
- (18) Peterson, K. A.; Werner, H. J. The Photodissociation of ClO_2 : Potential Energy Surfaces of $\text{OCIO} \rightarrow \text{Cl} + \text{O}_2$. *J. Chem. Phys.* **1996**, *105*, 9823–9832.
- (19) Werner, H.; Knowles, P. J. An Efficient Internally Contracted Multiconfiguration Reference CI Method. *J. Chem. Phys.* **1988**, *89*, 5803–5814.
- (20) Knowles, P. J.; Werner, H. J. An Efficient Method for the Evaluation of Coupling Coefficients in Configuration Interaction Calculations. *Chem. Phys. Lett.* **1988**, *145*, 514–522.
- (21) Werner, H.-J.; Knowles, P. J. A Second Order Multi-configuration SCF Procedure with Optimum Convergence. *J. Chem. Phys.* **1985**, *82*, 5053–5063.
- (22) Knowles, P. J.; Werner, H.-J. An Efficient Second Order MCSCF Method for Long Configuration Expansions. *Chem. Phys. Lett.* **1985**, *115*, 259–267.
- (23) Dunning, T. H., Jr. Gaussian Basis Sets for use in Correlated Molecular Calculations. I. The Atoms Boron through Neon and Hydrogen. *J. Chem. Phys.* **1989**, *90*, 1007–1023.
- (24) Kendall, R. A.; Dunning, T. H., Jr.; Harrison, R. J. Electron Affinities of the First-Row Atoms Revisited. Systematic Basis Sets and Wave Functions. *J. Chem. Phys.* **1992**, *96*, 6796–6806.
- (25) Tanaka, K.; Tanaka, T. CO_2 And N_2O Laser Stark Spectroscopy of the ν_1 Band of the ClO_2 Radical. *J. Mol. Spectrosc.* **1983**, *98*, 425–452.
- (26) Davis, H. F.; Lee, Y. T. Dynamics and Mode Specificity in OCIO Photodissociation. *J. Phys. Chem.* **1993**, *96*, 5681–5684.
- (27) Stert, V.; Ritze, H.-H.; Hertel, I. V.; Radloff, R. Ultrafast Processes in OCIO Molecules Excited by Femtosecond Laser Pulses at 389–409 nm. *J. Chem. Phys.* **2006**, *125*, 124312-1–124312-6.
- (28) Meng, Q.; Huang, M.-B. CASSCF And CASPT2 Study an O- and Cl-loss Predissociation Mechanisms of $\text{OCIO}(\text{A } ^2\text{A}_2)$. *J. Phys. Chem. A* **2011**, *115*, 2692–2701.
- (29) Andersson, K.; Roos, B. O. Multiconfigurational Second-Order Perturbation Theory: A Test of Geometries and Binding Energies. *Int. J. Quantum Chem.* **1993**, *45*, 591–607.
- (30) Almlof, J.; Taylor, P. R. General Contraction of Gaussian Basis Sets. I. Atomic Natural Orbitals for First- and Second-Row Atoms. *J. Chem. Phys.* **1987**, *86*, 4070–4077.
- (31) Widmark, P.-O.; Malmqvist, P.-A.; Roos, B. O. Density Matrix Averaged Atomic Natural Orbital (ANO) Basis Sets for Correlated Molecular Wave Functions. *Theor. Chim. Acta* **1990**, *77*, 291–306.

- (32) Widmark, P.-O.; Persson, B. J.; Roos, B. O. Density Matrix Averaged Atomic Natural Orbital (ANO) Basis Sets for Correlated Molecular Wave Functions. *Theor. Chem. Acc.* **1991**, *79*, 419–432.
- (33) Pierloot, K.; Dumez, B.; Widmark, P.-O.; Roos, B. O. Density Matrix Averaged Atomic Natural Orbital (ANO) Basis Sets for Correlated Molecular Wave Functions. *Theor. Chim. Acta* **1995**, *90*, 87–114.
- (34) Peterson, K. A.; Werner, H.-J. A Multireference Configuration Interaction Study of the Low-Lying Electronic States of ClO_2^+ and the X^1A_1 State of ClO_2^- . *J. Chem. Phys.* **1993**, *99*, 302–307.
- (35) Peterson, K. A. Accurate Ab Initio Near-Equilibrium Potential Energy and Dipole Moment Functions of the X^2B_1 and First Excited 2A_2 Electronic States of OCIO and OBrO . *J. Chem. Phys.* **1998**, *109*, 8864–8875.
- (36) Grant, D. J.; Garner, E. B., III; Matus, M. H.; Nguyen, M. T.; Peterson, K. A.; Francisco, J. S.; Dixon, D. A. Thermodynamic Properties of the XO_2 , X_2O , XO , X_2O_2 , and YXO_2 ($\text{X}, \text{Y} = \text{Cl}, \text{Br}$, and I) Isomers. *J. Phys. Chem. A* **2010**, *114*, 4254–4265.
- (37) Wei, Z.; Li, B.; Zhang, H.; Sun, C.; Han, K. A Theoretical Investigation of the Excited States of OCIO Radical, Cation, and Anion Using the CASSCF/CASPT2 Method. *J. Comput. Chem.* **2006**, *28*, 467–477.
- (38) Grein, F. Multireference Configuration Interaction Studies on Higher Valence and Rydberg States of OCIO , Ionization Potentials, and Electron Detachment Energies. *J. Chem. Phys.* **2011**, *135*, 044304.
- (39) Schäfer, A.; Huber, C.; Ahlrichs, R. Fully Optimized Contracted Gaussian Basis Sets of Triple Zeta Valence Quality for Atoms Li to Kr. *J. Chem. Phys.* **1994**, *100*, 5829–5835.
- (40) Fernández, B.; O, C.; Jørgensen, J.; Byberg, P.; Gauss, J.; Ruud, K. Hyperfine and Nuclear Quadrupole Coupling in Chlorine and Fluorine Dioxides. *J. Chem. Phys.* **1997**, *106*, 1847–1855.
- (41) Karton, A.; Parthiban, S.; Martin, J. M. L. Post-CCSD(T) Ab Initio Thermochemistry of Halogen Oxides and Related Hydrides XOX , XOOX , HOX , XO_n , and HXO_n ($\text{X} = \text{F}, \text{Cl}$), and Evaluation of DFT Methods for these Systems. *J. Phys. Chem. A* **2009**, *113*, 4802–4816.
- (42) Alcamí, M.; Mó, O.; Yáñez, M.; Cooper, I. L. The Performance of Density-Functional Theory in Challenging Cases: Halogen Oxides. *J. Chem. Phys.* **2000**, *112*, 6131–6140.
- (43) Beltrán, A.; Andrés, J.; Noury, S.; Silvi, B. Structure and Bonding of Chlorine Oxides and Peroxides: ClO_x , $\text{ClO}_x^-(x = 1 - 4)$, and $\text{Cl}_2\text{O}_x(x = 1 - 8)$. *J. Phys. Chem. A* **1999**, *103*, 3078–3088.
- (44) Li, Q.; Lü, S.; Xu, W.; Xie, Y.; Schaefer, H. F., III. Molecular Structures and Electron Affinities for the Chlorine Oxides ClOO , ClOOO , and $\text{ClO}_3(\text{C}_{3v})$. *J. Phys. Chem. A* **2002**, *106*, 12324–12330.
- (45) Zhu, R. S.; Lin, M. C. Ab Initio Studies of ClO_x Reactions. VIII. Isomerization and Decomposition of ClO_2 Radicals and Related Bimolecular Processes. *J. Chem. Phys.* **2003**, *119*, 2075–2082.
- (46) Jaffri, J. A.; Lengsfeld, B. H.; Bauschlicher, C. W.; Phillips, D. H. The Lower Electronic States of ClOO : A Computational Investigation. *J. Chem. Phys.* **1985**, *83*, 1693–1701.
- (47) Suma, K.; Sumiyoshi, Y.; Endo, Y. Fourier Transform Microwave Spectroscopy and Fourier Transform Microwave–Millimeter Wave Double Resonance Spectroscopy of the ClOO Radical. *J. Chem. Phys.* **2004**, *121*, 8351.
- (48) Suma, K.; Sumiyoshi, Y.; Endo, Y.; Enami, S.; Aloisio, S.; Hashimoto, S.; Kawasaki, M. Equilibrium Constants of the Reaction of Cl with O_2 in the Formation of ClOO . *J. Phys. Chem. A* **2004**, *108*, 8096–8099.
- (49) Grein, F. Theoretical Studies on ClOO : Electronic Spectra, Ionization Potential, and Electron Affinity. *Can. J. Phys.* **2011**, *89*, 891–897.
- (50) Martin, J. M. L.; de Oliveira, G. Towards Standard Methods for Benchmark Quality Ab Initio Thermochemistry: W1 and W2 Theory. *J. Chem. Phys.* **1999**, *111*, 1843–1856.
- (51) Boese, A. D.; Oren, M.; Atasoylu, O.; Martin, J. M. L.; Kállay, M.; Gauss, J. W3 Theory: Robust Computational Thermochemistry in the kJ/mol Accuracy Range. *J. Chem. Phys.* **2006**, *120*, 4129–4141.
- (52) Karton, A.; Rabinovich, E.; Martin, J. M. L.; Ruscic, B. W4 Theory for Computational Thermochemistry: In Pursuit of Confident Sub-kJ/mol Predictions. *J. Chem. Phys.* **2006**, *125*, 144108.
- (53) Karton, A.; Taylor, P. R.; Martin, J. M. L. Basis Set convergence of Post-CCSD Contributions to Molecular Atomization Energies. *J. Chem. Phys.* **2007**, *127*, 064104.
- (54) Mebel, A. M.; Morokuma, K.; Lin, M. C. Modification of the Gaussian - 2 Theoretical Model: The Use of Coupled-Cluster Energies, Density-Functional Geometries, and Frequencies. *J. Chem. Phys.* **1995**, *103*, 7414–7421.
- (55) Mueller, H. S. P.; Willner, H. Vibrational and Electronic Spectra of Chlorine Dioxide, OCIO , and Chlorine Superoxide ClOO , Isolated in Cryogenic Matrices. *J. Phys. Chem.* **1993**, *97*, 10589–10598.
- (56) Chase, Jr., M. W. *NIST-JANAF Thermochemical Tables*, 4th ed.; AIP: Woodbury, NY, 1998.
- (57) Varandas, A. J. C. A General Approach to the Potential Energy Functions of Small Polyatomic Systems: Molecules and van der Waals Molecules. *J. Mol. Struct.: THEOCHEM* **1985**, *120*, 401–424.
- (58) Varandas, A. J. C. Intermolecular And Intramolecular Potentials: Topographical Aspects, Calculation, and Functional Representation via a DMBE Expansion Method. *Adv. Chem. Phys.* **1988**, *74*, 255–338.
- (59) Varandas, A. J. C. A New Formulation of Three-Body Dynamical Correlation Energy for Explicit Potential Functions. *Chem. Phys. Lett.* **1992**, *194*, 333–340.
- (60) Varandas, A. J. C. Chapter Multivalued Potential Energy Surfaces for Dynamics Calculations. In *Lecture Notes in Chemistry*; Laganá, A., Riganelli, A., Eds.; Springer: Berlin, 2000; Vol. 75, pp 33–56.
- (61) Varandas, A. J. C. Combined-Hyperbolic-Inverse-Power-Representation of Potential Energy Surfaces: A Preliminary Assessment for H_3 and HO_2 . *J. Chem. Phys.* **2013**, *138*, 054120.
- (62) Werner, H.-J.; Knowles, P. J.; Knizia, G.; Manby, F. R.; Schütz, M.; Celani, P.; Korona, T.; Lindh, R.; Mitrushenkov, A.; Rauhut, G. et al. *MOLPRO*, version 2010.1, a Package of Ab Initio Programs, 2010 (<http://www.molpro.net>, see <http://www.molpro.net>).
- (63) Varandas, A. J. C.; Piecuch, P. Extrapolating Potential Energy Surfaces by Scaling Electron Correlation at a Single Geometry. *Chem. Phys. Lett.* **2006**, *430*, 448–453.
- (64) Varandas, A. J. C. Accurate Global Ab Initio Potentials at Low-Cost by Correlation Scaling and Extrapolation to the One-Electron Basis Set Limit. *Chem. Phys. Lett.* **2007**, *443*, 398–407.
- (65) Varandas, A. J. C. Extrapolating to the One-Electron Basis-Set Limit in Electronic Structure Calculations. *J. Chem. Phys.* **2007**, *126*, 244105.
- (66) Varandas, A. J. C. Accurate Ab Initio-Based Molecular Potentials: From Extrapolation Methods to Global Modelling. *Phys. Scr.* **2007**, *76*, C28–C35.
- (67) Varandas, A. J. C. Accurate Ab Initio Potentials at Low Cost via Correlation Scaling and Extrapolation: Application to $\text{CO}(A^1\Pi)$. *J. Chem. Phys.* **2007**, *127*, 114316.
- (68) Song, Y.; Varandas, A. J. C. Accurate Ab Initio Double Many-Body Expansion Potential Energy Surface for Ground-State H_2S by Extrapolation to the Complete Basis Set Limit. *J. Chem. Phys.* **2009**, *130*, 134317.
- (69) Varandas, A. J. C. Extrapolation to the Complete Basis Set Limit Without Counterpoise. The Pair Potential of Helium Revisited. *J. Phys. Chem. A* **2010**, *114*, 8505–8516.
- (70) Varandas, A. J. C. Helium-Fullerene Pair Interactions: An Ab Initio Study by Perturbation Theory and Coupled Cluster Methods. *Int. J. Quantum Chem.* **2011**, *111*, 416–429.
- (71) Jensen, F. Estimating the Hartree-Fock Limit from Finite Basis Set Calculations. *Theor. Chem. Acc.* **2005**, *113*, 267–273.
- (72) Karton, A.; Martin, J. Comment on: “Estimating the Hartree-Fock limit from finite basis set calculations” [Jensen, F. *Theor. Chem. Acc.* 2005, 113, 267]. *Theor. Chem. Acc.* **2006**, *115*, 330–333.
- (73) Varandas, A. J. C.; Silva, J. D. Potential Model for Diatomic Molecules Including the United-Atom Limit and its Use in a Multiproperty Fit for Argon. *J. Chem. Soc., Faraday Trans.* **1992**, *88*, 941–954.

- (74) Varandas, A. J. C. On The Relation of Dispersion to Induction Energies, and to Their Damping Functions. Ion-Atom Potentials: The $X^2\Sigma_g^+$ and $1^2\Sigma_u^+$ of H_2^+ . *Mol. Phys.* **1987**, *60*, 527–539.
- (75) Pastrana, M. R.; Quintales, L. A. M.; Brandão, J.; Varandas, A. J. C. Recalibration of a Single-Valued Double Many-Body Expansion Potential-Energy Surface for Ground-State HO_2 and Dynamics Calculations for the $O + OH \rightarrow O_2 + H$ Reaction. *J. Phys. Chem.* **1990**, *94*, 8073–8080.
- (76) Peña-Gallego, A.; Abreu, P. E.; Varandas, A. J. C. MRCI Calculation, Scaling of the External Correlation, and Modeling of Potential Energy Curves for HCl and OCl. *J. Phys. Chem. A* **2000**, *104*, 6241–6246.
- (77) Le Roy, R. J. Energy Levels of a Diatomic Near Dissociation. In *Molecular Spectroscopy I (A Specialist Periodical Report of the Chemical Society of London)*; Barrow, R. F., Long, D. A., Millen, D. J., Eds.; Chemical Society of London, 1973; Vol. 1, pp 113–176.
- (78) Varandas, A. J. C. Energy Switching Approach to Potential Energy Surfaces: An Accurate Single-Valued Function for the Water Molecule. *J. Chem. Phys.* **1996**, *105*, 3524–3531.
- (79) Varandas, A. J. C. Double Many-Body Expansion of Molecular Potential Energy Functions and the Role of Long-Range Forces in the Rates of Chemical Reactions. *J. Mol. Struct.: THEOCHEM* **1988**, *166*, 59–74.
- (80) Matas, M. A.; Varandas, A. J. C. Atom-Molecule Dispersion Coefficients and Their Dependence on the Intramolecular Coordinate: $A - H_2$ Systems. *Mol. Phys.* **1990**, *70*, 623–644.
- (81) Varandas, A. J. C.; Pais, A. A. C. C. A Realistic Double Many-Body Expansion (DMBE) Potential Energy Surface for Ground-State O_3 from a Multiproperty Fit to Ab Initio Calculations, and to Experimental Spectroscopic, Inelastic Scattering, and Kinetic Isotope Thermal Rate Data. *Mol. Phys.* **1988**, *65*, 843–860.
- (82) Buckingham, A. D. Permanent and Induced Molecular Moments and Long-Range Intermolecular Forces. *Adv. Chem. Phys.* **1967**, *12*, 107–142.
- (83) Varandas, A. J. C.; Brandão, J.; Quintales, A. M. A Realistic $HO_2(\tilde{X}^2A'')$ Potential Energy Surface from the Double Many-Body Expansion Method. *J. Phys. Chem.* **1988**, *92*, 3732–3742.
- (84) Varandas, A. J. C.; Rodrigues, S. P. J. Double Many-Body Expansion Potential Energy Surface for Ground-State HCN Based on Realistic Long Range Forces and Accurate Ab Initio Calculations. *J. Chem. Phys.* **1997**, *106*, 9647–9658.
- (85) Rodrigues, S. P. J.; Varandas, A. J. C. On the Variation of the Electric Quadrupole Moment with Internuclear Distance. *Phys. Chem. Chem. Phys.* **2000**, *2*, 435–439.
- (86) Rodrigues, S. P. J.; Sabn, J. A.; Varandas, A. J. C. Single-Valued Double Many-Body Expansion Potential Energy Surface of Ground-State SO_2 . *J. Phys. Chem. A* **2002**, *106*, 556–562.
- (87) Martinez-Núñez, E.; Varandas, A. J. C. Single-Valued DMBE Potential Energy Surface for HSO: A Distributed n -Body Polynomial Approach. *J. Phys. Chem. A* **2001**, *105*, 5923–5932.
- (88) Curtiss, L. A.; Raghavachari, K.; Redfern, P. C.; Pople, J. A. Assessment of Gaussian-2 and Density Functional Theories for the Computation of Enthalpies of Formation. *J. Chem. Phys.* **1997**, *106*, 1063–1079.